

The detection and photometric redshift determination of distant galaxies using *SIRTF*'s Infrared Array Camera

Chris Simpson and Peter Eisenhardt

Jet Propulsion Laboratory, California Institute of Technology, Mail Stop 169-327, 4800
Oak Grove Drive, Pasadena, CA 91109

ABSTRACT

We investigate the ability of the *Space Infrared Telescope Facility*'s Infrared Array Camera to detect distant ($z \sim 3$) galaxies and measure their photometric redshifts. Our analysis shows that changing the original long wavelength filter specifications provides significant improvements in performance in this and other areas.

1. Introduction

On 1998 March 25, NASA Administrator Daniel Goldin approved the initiation of final design and construction for the *Space Infrared Telescope Facility* (*SIRTF*; Fanson et al. 1998). With launch planned for December 2001, *SIRTF* will complete NASA's family of Great Observatories. *SIRTF* will provide a large increase in sensitivity over previous missions across its 3–200 μm operating range, and over 75% of the observing time during its 2.5 year-minimum lifetime will be awarded to general investigators.

One of the defining scientific programs for *SIRTF* is the study of distant galaxies by means of deep surveys at 3–10 μm . Not only will *SIRTF*'s excellent sensitivity in this wavelength region allow such galaxies to be detected with the Infrared Array Camera (IRAC; Fazio et al. 1998), but the H^- opacity minimum at 1.6 μm is expected to be a major tool in photometric redshift determination at $1 \lesssim z \lesssim 5$ (Wright, Eisenhardt & Fazio 1994). The rest frame 1–2 μm spectral region is also of particular importance because its luminosity correlates linearly with mass (Gavazzi, Pierini & Boselli 1996).

IRAC will have two detector arrays made from indium antimonide (InSb) which is sensitive to $\lambda \lesssim 5 \mu\text{m}$ photons, and two made from arsenic-doped silicon (Si:As) which detects longer-wavelength light. All four arrays will have a 256×256 format, with $1''.2$ pixels, and will operate simultaneously. The InSb arrays will have filters centered at 3.63 μm with 20.4% bandwidth and at 4.53 μm with 23.3% bandwidth. We shall refer to these filters as L

and M , respectively, because of their similarity to the filters used in ground-based facilities. The filters for the Si:As arrays have no ground-based analogs, and so we refer to them as A and B , with A being the bluer of the two. The L and A filters share one field and are separated by a dichroic filter, while the M and B filters similarly share a second nearly adjacent field. The original, or “baseline”, specifications for A and B are 25% bandwidth filters centered at 6.3 and $8.0\,\mu\text{m}$.

In this paper we examine changing the specifications of the Si:As filters in order to optimize them for the study of $z \sim 3$ galaxies. UV-bright examples of such galaxies have already been detected by means of the “UV dropout” technique (Steidel & Hamilton 1992, 1993; Steidel et al. 1996) and they play an important role in the overall star formation history of the Universe (Madau et al. 1996). We focus on both the ability to detect these objects, and the accuracy with which their redshifts can be estimated from their colors in the IRAC filters. Our analysis will involve comparing the performance of different pairs of filters, and we distinguish between these pairs by the use of subscripts, so for example the baseline filters described above are called A_b and B_b . We also introduce the notation $[\lambda_1 : \lambda_2]$ to describe a filter which extends from $\lambda_1\,\mu\text{m}$ to $\lambda_2\,\mu\text{m}$. In this notation, the L filter is $[3.26 : 4.00]$, $M = [4.00 : 5.06]$, $A_b = [5.51 : 7.09]$, and $B_b = [7.00 : 9.00]$.

2. Assumptions

The calculations in this paper all assume a total integration time of 10 hours per point (made up of many individual 200 second exposures), which allows a deep image of a large area of sky to be obtained in a sensible integration time. For such exposure times, IRAC requires background-limited operation and therefore we neglect read noise and dark current. Confusion noise will be discussed in §5.1. but is otherwise not considered here. As *SIRTF* is required to be diffraction limited at $6.5\,\mu\text{m}$, we adopt a detection area of twenty pixels, independent of wavelength, and assume that all the source flux is contained within this region.

2.1. Telescope and instrument efficiency

The fraction of photons incident upon *SIRTF*’s 85 cm diameter aperture which reach the IRAC detectors is specified in the *SIRTF* Observatory Performance and Interface

Control Document and the IRAC Instrument Performance Requirements Document¹, and is about 50%, including filter transmission. The InSb quantum efficiency (QE) is assumed to be 80% over the entire wavelength range of the two InSb filters, whereas the Si:As QE varies with wavelength, rising from $\sim 17\%$ at $5\mu\text{m}$ to a peak of 40% at $\sim 15\mu\text{m}$. We assume that the various filters considered here are opaque outside their nominal wavelength region.

2.2. Background

From the PICD, the minimum *SIRTF* background (which occurs at the ecliptic pole for wavelengths considered here), $b(\lambda)$ is computed as

$$b(\lambda) = 1.9 \times 10^{-13} B_{\lambda}(5500) + 4.0 \times 10^{-8} B_{\lambda}(278.5) + 1.78 \times 10^{-5} B_{\lambda}(24.45) + B_{\lambda}(2.73),$$

where $B_{\lambda}(T)$ is the Planck function for a temperature of T K. The first term is due to scattered sunlight from zodiacal dust, the second and third terms to thermal emission from zodiacal and Galactic dust, respectively, and the final term is the cosmic microwave background radiation. This function provides an excellent fit to data from the DIRBE instrument (Hauser 1996).

2.3. Cosmology and galaxy models

Our analysis is concerned with the detection of high redshift galaxies. We construct model spectra of such galaxies using the GISSSEL96 spectral synthesis code (Bruzual & Charlot 1993, 1998; see also Charlot, Worthey & Bressan 1996). This code does not include polycyclic aromatic hydrocarbon (PAH) features at $3.3\mu\text{m}$ and beyond, but at $z = 3$ these features are at observed wavelengths beyond the range considered here. We will return to the PAH features when we discuss confusion noise.

We adopt a conservative (in the sense of making $z \sim 3$ galaxies faint) cosmology with $H_0 = 50 \text{ km s}^{-1} \text{ Mpc}^{-1}$ and $q_0 = 0.1$, corresponding to a present age of the Universe of 16.5 Gyr (at $z = 3$ the Universe is 2.9 Gyr old). We assume a Salpeter (1955) IMF extending from 0.1 – $125 M_{\odot}$, and normalize our galaxies to have $M_K = -25.1$ (L^* ; Mobasher, Sharples & Ellis 1993) at an age of 16.5 Gyr. We use four models to represent the limits

¹The PICD is Jet Propulsion Laboratory document 674-SEIT-100, V2.2. The IPRD is Smithsonian Astrophysical Observatory document IRAC96-202, revision 4.2.

of galaxy evolution. Model A is a maximally old model with solar metallicity formed in an instantaneous burst at $z = \infty$ and evolving passively thereafter. Model B is like A but with metallicity only $\frac{1}{50}$ solar. Model C is a young solar metallicity galaxy formed with a constant star formation rate over the 100 Myr prior to whatever redshift is considered (i.e. a young nonevolving spectrum). Model D is like C, but again with $Z = 0.02Z_{\odot}$. Models C and D are much more luminous than models A and B at $z = 3$. The rest frame 0.5–5 μm spectra of these models at $z = 3$ are shown in Figure 1.

3. Sensitivity

Since *SIRTF*’s observations will be dominated by general observer programs, it is important to consider performance independent of any particular program, in addition to the high redshift galaxy observations which drive the filter recommendations made here. In fact, as we discuss in §6., the pair of filters which provide the optimum performance for $A - B$ color selection and photometric redshift determination at $z \sim 3$ are not very suitable for other science programs. For this reason we will throughout the course of this paper be discussing the relative performance of three different Si:As filter pairs, which we designate “baseline”, “optimum”, and “preferred” and denote by subscripts b , o , and p , respectively. The baseline filters are the two 25% bandwidth filters centered at 6.3 and 8.0 μm , the optimum filters provide the most accurate $A - B$ color selection and photometric redshift determination (see §4.) at $z \sim 3$, and the preferred filters give slightly poorer performance in these areas, but are expected to be much more useful for other scientific programs. The optimum filters are $A_o = [5.06 : 6.00]$ and $B_o = [6.40 : 10.30]$, and the preferred filters are $A_p = [5.06 : 6.50]$ and $B_p = [6.50 : 9.50]$.

3.1. Power law spectrum source

Figure 2 is a contour plot of IRAC’s background limited 5σ sensitivity in 10 hours of integration as a function of filter cuton and cutoff wavelength for a source which has a flat spectrum in S_{ν} . Since the contour lines are fairly vertical, it is evident that the cuton wavelength is more important than the cutoff. It is also clear from this figure that the best sensitivity is achieved for a very blue filter whose short wavelength cuton will be constrained by the dichroic response. Within the parameter space plotted, a $[4.2 : 5.7]$ filter is most sensitive, with a 5σ 10 hr limiting flux of 1.1 μJy . However, this filter overlaps the InSb M filter almost entirely, and since InSb has a much higher quantum efficiency there is little point in duplicating it. We therefore restrict our analysis to filters with $\lambda_{\text{cuton}} > 5.06 \mu\text{m}$

(the cutoff of the M filter). The second column in Table 1 lists the sensitivity achieved by various IRAC filters for a flat spectrum source. The most sensitive Si:As filter is $[5.06 : 7.4]$ but, as remarked above, the sensitivity is largely independent of the cutoff wavelength, dropping only 1% if we reduce the cutoff to $7\,\mu\text{m}$ or raise it to $8.3\,\mu\text{m}$.

The optimum and preferred filters have a $\sim 20\%$ gain in sensitivity over the baseline specifications for a flat spectrum source. Figure 3 shows that the improvement holds for a fairly large range of spectral shapes, with the preferred A_p filter only losing out to the baseline A_b filter for spectra redder than $\alpha \gtrsim 2$ ($S_\nu \propto \nu^{-\alpha}$), due to the longer wavelength of the A_b filter.

3.2. High redshift galaxies

Figure 4 plots the SNR achievable in 10 hours through Si:As filters for the four galaxy models at $z = 3$. Again the contours are fairly vertical showing the cuton wavelength is important and the SNR achievable is very insensitive to the cutoff. The best SNR at $z = 3$ for the Si:As filter is again with the bluest wavelength cuton allowed ($5.06\,\mu\text{m}$) and with a cutoff of 7.4, 6.1, 7.2, and $6.7\,\mu\text{m}$ for models A, B, C, and D, respectively. Table 1 lists the signal-to-noise ratios achievable at $z = 3$ for the various Si:As filter choices.

The general conclusions thus far are that substantial improvements in sensitivity can be achieved over the baseline filter specifications by using a bluer A filter and a broader B filter. We show that this applies over a broad range of redshift in Figures 5 and 6, which plot the signal-to-noise ratio achievable in 10 hours for the three different filter pairs. For completeness, we show the SNR achievable through the two InSb filters as a function of redshift in Figure 7. The higher quantum efficiency of InSb and the lower background at short wavelengths produce an order of magnitude increase over what is achievable with the two Si:As arrays, but the need for the Si:As arrays will become clear in the next section.

4. Photometric redshift determination at $z \sim 3$

In this section we present the analysis which defines the “optimum” filters and leads to our specifications for the “preferred” filters.

Two factors are important in deciding upon the best filters for photometric redshift determination. First, it is necessary to achieve a high signal-to-noise ratio in both filters, to allow the color to be determined accurately. This was discussed in the previous section.

Secondly, this color must be a strong function of redshift, since the uncertainty in redshift, Δz , is related to the uncertainty in the color, $\Delta\Gamma$ (the color defined in the sense $\Gamma \equiv A - B$) by

$$\Delta z = (d\Gamma/dz)^{-1} \Delta\Gamma. \quad (1)$$

Figure 8 plots the $L - B$, $M - B$, and $A - B$ colors as a function of redshift for the four models. Magnitudes in each of the filters have been determined with respect to Vega (which we model as a 9400 K blackbody with a $2.2\mu\text{m}$ flux of 657 Jy). It should be noted that at $z \lesssim 2$, the $3.3\mu\text{m}$ PAH feature may affect the results since it will lie in the bandpass of filter B . It is apparent that the $L - M$ color is sensitive to redshift in the range $1 < z < 2$, due to the $1.6\mu\text{m}$ bump moving through the filters. At higher redshifts the Si:As filters become increasingly important for measuring photometric redshifts. At $z > 2$, the increased separation between the preferred and optimum A and B filters, compared to the baseline filters, causes them to produce larger color variations. Coupled with the increased sensitivity that these filters provide, it is clear that they will be able to produce more accurate photometric redshifts. We now quantify the level of this improvement.

The goal of photometric redshift determination is to minimize the uncertainty in the derived redshift, given by Equation 1. We make a few approximations to ease the calculation of this function. First, we write $d\Gamma/dz \approx \Gamma(3.5) - \Gamma(2.5)$, and make use of the fact that for well-detected ($\gtrsim 5\sigma$) sources, the uncertainty in the measured magnitude $\Delta m \approx (\text{SNR})^{-1}$, where SNR is the signal-to-noise ratio. We approximate the SNR (which varies slightly with redshift) as the geometric mean of the actual SNR at $z = 2.5$ and $z = 3.5$. In light of these rather crude approximations, we do not claim to be deriving accurate values of Δz , but instead present its reciprocal, which we call f (by plotting the reciprocal, we also avoid the infinities which arise when the color change between $z = 2.5$ and $z = 3.5$ is zero). For any two filters, X and Y , f is therefore defined as

$$f(X, Y) = \frac{\Gamma(3.5) - \Gamma(2.5)}{\left(\frac{b_X}{c_X(3.5)c_X(2.5)} + \frac{b_Y}{c_Y(3.5)c_Y(2.5)} \right)^{1/2}}, \quad (2)$$

where b_i is the total number of background counts and $c_i(z)$ the total number of object counts in filter i for a galaxy at redshift z . Large values of f are desired, and for photometric redshifts accurate to 10% at $z \sim 3$ ($\Delta z \lesssim 0.3$), $f \gtrsim 3$ is necessary.

We wish to find the specifications for the two Si:As filters that maximize $f(A, B)$. Unfortunately, since each filter needs two parameters to specify it, it is impossible to graphically present the results of this four-parameter optimization in a simple form. We therefore first consider the value of f for a single Si:As filter and the InSb M filter (the results are broadly similar if the L filter is used instead of M). Figure 9 is a contour plot

of f for the M filter and an arbitrary Si:As filter whose specifications are given by the two axes. This figure favors a Si:As filter centered at $\sim 8\mu\text{m}$ with $\sim 50\%$ bandwidth. Note that the contours are predominantly horizontal here, so that contrary to the SNR case, the long wavelength cutoff is the most important parameter. A broad, long wavelength filter is optimum for determining photometric redshifts at $z \sim 3$ even though the SNR it produces is not maximal.

We find the solution to the four-parameter optimization by performing a grid search throughout the available parameter space. We find that, irrespective of the particular galaxy model, the A filter always has the bluest cuton allowed ($5.06\mu\text{m}$). This is to be expected, since a blue A filter produces both high signal-to-noise (Figures 2 and 4) and a large color change over the redshift range of interest. The other parameters vary slightly between the four galaxy models, but an average solution is $A = [5.06 : 6.0]$ and $B = [6.4 : 10.3]$. This is how we define the “optimum” filter choice referred to throughout this paper. The optimum B filter has a similar specification regardless of whether the color is formed using L , M , or A as the second filter.

Table 2 lists the values of f achieved for various pairs of filters. In terms of the value of this function, the optimum filters can produce an increase of as much as 60% in the accuracy of the photometric redshifts derived from the A and B filters, and a more modest (but still substantial) 20% improvement in accuracy when one of the InSb filters is used in conjunction with the B filter.

In order to give the reader some feeling for the variation of f with filter specifications, we present the variation of f along planes of the four-dimensional parameter space that defines the two Si:As filters. We do this by specifying two constraints on the filter properties. Figure 10 shows the contours of f for the case where both filters have a 25% bandwidth. In Figure 11 the filter A cuton has been set to $5.06\mu\text{m}$ and its cutoff is equal to the filter B cuton.

As an illustration of how photometric redshifts might be derived from IRAC data, in Figure 12 we present a $L - M$ vs $A_p - B_p$ color-color plot for the four galaxy models in the redshift range $1 < z < 5$. It can be seen that the color in the two Si:As filters is generally able to provide an excellent measurement of the galaxy redshift for $z \gtrsim 2$. For $1 \lesssim z \lesssim 2$, the $L - M$ color provides most of the photometric redshift signal.

5. Other considerations

Finally, we consider the impact of filter changes on two important aspects of distant galaxy detection which we have thus far ignored: confusion noise, which will ultimately limit *SIRTF*'s sensitivity, and dust, which is not included in the Bruzual & Charlot spectral synthesis models.

5.1. Confusion noise

Confusion noise is expected to limit IRAC sensitivity to $\sim 0.5 \mu\text{Jy}$ (1σ), and depends on the source density and the beam size, both of which are wavelength dependent. Of particular concern is how much the density of confusing sources will increase with a new *B* filter, which is both more sensitive, and has a longer cutoff wavelength, than the baseline filter. The longer cutoff may significantly increase confusion because it includes the strong, broad $7.7 \mu\text{m}$ PAH feature (e.g. Uchida, Sellgren & Werner 1998) out to $z \sim 0.5$, a large enough distance that substantial volume is sampled and evolving dwarf galaxies may dominate the counts.

Franceschini et al. (1991) estimate the density of sources at $6.7 \mu\text{m}$. At microJansky flux levels, most sources will be at $z \gtrsim 1$, so we use the spectrum $S_\nu \propto \nu^{-0.3}$ displayed at rest wavelengths $\sim 3 \mu\text{m}$ to convert a limiting $8 \mu\text{m}$ flux to a $6.7 \mu\text{m}$ flux. Our best estimate of the total number of sources above $0.5 \mu\text{Jy}$ at $8 \mu\text{m}$ is therefore $\sim 100 \text{ arcmin}^{-2}$, which is ~ 0.8 sources per 20 pixel detection area. We estimate the number of PAH-emitting galaxies from the cirrus/photodissociation region spectrum and local $15 \mu\text{m}$ luminosity function of Xu et al. (1998). Even with very strong $((1+z)^4)$ evolution, the number of sources with $z < 0.5$ above $0.5 \mu\text{Jy}$ is no more than 10 arcmin^{-2} , a small fraction of the total confusing source density.

Calculations (Gautier, private communication) show that convolving the diffraction limited beam with a range of spectral slopes shows no significant change in beam size for the preferred *B* filter over the baseline specifications. Therefore the performance of the B_p filter will not be compromised as a result of significantly increased confusion noise.

5.2. Dusty galaxies

Nearby starburst galaxies, e.g. M 82 and Arp 220, are very dusty and have red near-infrared spectra, as well as strong PAH emission features. Our choice of a bluer *A* filter might therefore impair our ability to detect similar objects at high redshift, which would be cosmologically very interesting. Figure 3(b) shows that for spectra redder than $\alpha \gtrsim 2$,

the A_b filter is more sensitive than A_p . In Figure 13 we show the sensitivities of the three different filter pairs to these two starburst galaxies as a function of redshift (the spectrum of M 82 has been scaled up by a factor of 10 in luminosity in this figure). The spectral energy distributions required to make these figures were produced with photometric data culled from a variety of sources, and aperture matching using curve-of-growth analysis was required. This is likely to produce errors where the spectral region sampled by a given filter includes the transition between different datasets (e.g. optical and near-infrared), and the signal-to-noise ratios (both absolute and relative) should probably not be trusted to more than $\sim 10\%$. From these figures, it is clear that there is little to choose between the different A filters, but the sensitivity improvement offered by the B_p filter is unambiguous.

6. Conclusions: the “preferred” filters

Although the broad B_o filter is supported by sensitivity calculations and does not suffer significantly from increased confusion noise, a somewhat narrower filter makes sense for other reasons. The almost 50% bandwidth of the B_o filter will make photometry difficult and may compromise other uses of this filter. In particular, the strong silicate absorption feature at $9.7\mu\text{m}$ falls in the B_o bandpass. We therefore recommend a shorter cutoff wavelength, and propose $B = [6.5 : 9.5]$ (a 37% bandpass) as our “preferred” B filter, B_p .

Conversely, the optimum $A_p = [5.06 : 6.0]$ choice is only a 17% bandwidth, and does not produce optimum SNR (see Table 1). It does however avoid the PAH feature at $6.2\mu\text{m}$, offering the possibility of using filters A and B as a PAH diagnostic. However the M filter also acts as a good continuum filter for this problem, with better SNR and the advantage that it shares the same field as the B filter. Hence we recommend a broader A filter filling the wavelength regime between M and B . Our preferred A filter, A_p , is then $[5.06 : 6.5]$, with a 25% bandpass.

These preferred filters reduce the value of f by about 10%, compared to the optimum filters, but we feel that this is outweighed by the gain in general scientific usefulness. In any case, they still offer a significant improvement over the baseline 6.3 and 8.0 filters. These specifications have now been adopted for the IRAC instrument.

Acknowledgments

The authors wish to thank Roc Cutri, Nick Gautier, Craig McCreight, and Harvey Moseley for their help. This work was performed by the Jet Propulsion Laboratory,

California Institute of Technology, under a contract with NASA.

REFERENCES

- Bruzual A., G., & Charlot S. 1993, *ApJ*, 405, 538
- Bruzual A., G., & Charlot S. 1998, in preparation
- Charlot, S., Worthey, G., & Bressan, A. 1996, *ApJ*, 457, 625
- Fanson, J., Fazio, G., Houck, J., Kelly, T., Rieke, G., Tenerelli, D., & Whitten, M. 1998, in *Space Telescopes and Instruments V*, *Proc. SPIE* 3356, in press
- Fazio, G., et al. 1998, in *Infrared Astronomical Instrumentation*, *Proc. SPIE* 3354, in press
- Franceschini, A., Toffolatti, L., Mazzei, P., Danese, L., & De Zotti, G. 1991, *A&AS*, 89, 285
- Gavazzi, G., Pierini, D., & Boselli, A. 1996, *A&A*, 312, 397
- Hauser, M. G., 1996, in *AIP Conf. Proc.* 348, *Unveiling the Cosmic Infrared Background*, ed. E. Dwek, (American Institute of Physics, Woodbury, New York), 11
- Madau, P., Ferguson, H. C., Dickinson, M. E., Giavalisco, M., Steidel, C. C., & Fruchter, A. 1996, *MNRAS*, 283, 1388
- Mobasher, B., Sharples, R. M., & Ellis, R. S. 1993, *MNRAS*, 263, 560
- Salpeter, E. E., 1955, *ApJ*, 121, 161
- Steidel, C. C., & Hamilton, D. 1992, *AJ*, 104, 941
- Steidel, C. C., & Hamilton, D. 1993, *AJ*, 105, 2017
- Steidel, C. C., Giavalisco, M., Pettini, M., Dickinson, M., & Adelberger, K. L. 1996, *ApJ*, 462, L17
- Uchida, K. I., Sellgren, K., & Werner, M. 1998, *ApJ*, 493, L109
- Wright, E. L., Eisenhardt, P., & Fazio, G. 1994, *AAS*, 26, 893
- Xu, C., Hacking, P. B., Fang, F., Shipe, D. L., Lonsdale, C. J., Lu, N. Y., & Helou, G. 1998, *ApJ*, submitted

Fig. 1.— The rest-frame spectra at $z = 3$ of the four galaxy models. The solid horizontal bars indicate the preferred filter set, while the dashed bars show the optimum Si:As filters and the dotted bars the baseline Si:As filters.

Fig. 2.— Contours of limiting flux in μJy (5σ , 10 hours) as a function of filter cuton and cutoff wavelength for a source with a flat spectrum (in S_ν). The contour range is from 1.2 to $5.0 \mu\text{Jy}$ in steps of $0.2 \mu\text{Jy}$. Squares mark the preferred filter specifications, triangles the optimum filters, and circles the baseline filters.

Fig. 3.— Limiting sensitivity (5σ , 10 hours) for the preferred (solid line), optimum (dashed line), and baseline (dotted line) filters for power laws of the form $S_\nu \propto \nu^{-\alpha}$. Left: Filter *A*. Right: Filter *B*.

Fig. 4.— Contours of signal-to-noise ratio as a function of filter cuton and cutoff in a 10 hour integration on the four galaxy models at $z = 3$. Symbols mark the filter specifications as in Figure 2. Model A is contoured from 2 to 30 in steps of 2; Model B from 2 to 25 in steps of 1; Model C from 20 to 360 in steps of 20; and Model D from 10 to 150 in steps of 10.

Fig. 5.— Signal-to-noise ratio (in 10 hours) for the three different *A* filters, as a function of redshift for the four galaxy models. Solid line: preferred (A_p); dashed line: optimum (A_o); dotted line: baseline (A_b).

Fig. 6.— As Figure 5, but for the three *B* filters.

Fig. 7.— As Figure 5, but for the InSb *L* (solid line) and *M* (dashed line) filters.

Fig. 8.— Colours as a function of redshift for the four galaxy models. Solid lines: preferred filters; dashed lines: optimum filters; dotted lines: baseline filters.

Fig. 9.— Contours of f (as defined in the text) for the InSb *M* filter and an arbitrary Si:As filter as defined by the axes of the plot, for each of the four galaxy models. Model A is contoured from -0.4 to 7.0 in steps of 0.2; Model B from 0.0 to 3.5 in steps of 0.1; Model C from -16 to 66 in steps of 2; and Model D from -1.2 to 7.4 in steps of 0.2.

Fig. 10.— Contours of f for two Si:As filters of 25% bandwidth, as a function of filter center. Model A is contoured from -0.2 to 5.6 in steps of 0.2; Model B from 0.0 to 2.8 in steps of 0.1; Model C from -2 to 60 in steps of 2; and Model D from -0.4 to 6.0 in steps of 0.2.

Fig. 11.— Contours of f for the case where filter A cuts on at $5.06\mu\text{m}$ and cuts off at the cuton wavelength of filter B . Model A is contoured from 1.0 to 6.0 in steps of 0.2; Model B from 0.4 to 2.8 in steps of 0.1; Model C from 12 to 62 in steps of 2; and Model D from 1.0 to 7.0 in steps of 0.2.

Fig. 12.— Loci of the four galaxy models discussed in the text in the $L - M$ vs $A_p - B_p$ color-color diagram. The locations of the models at $z = 1, 2, 3, 4, 5$ are indicated.

Fig. 13.— Signal-to-noise ratio (in 10 hours) for redshifted versions of the starburst galaxies M 82 and Arp 220. M 82 has been scaled up by a factor of 10 in luminosity. Solid lines: preferred filters; dashed lines: optimum filters; dotted lines: baseline filters.

Table 1: Signal-to-noise achievable in 10 hours of integration for a $10\mu\text{Jy}$ flat spectrum source and the four galaxy models at $z = 3$. The “best filter” is the most sensitive for each model, with the constraint that no filter extends bluer than $5.06\mu\text{m}$. All such filters cut on at $5.06\mu\text{m}$ and extend to the cutoff wavelength listed.

Filter	SNR for Model				
	$10\mu\text{Jy}$	A	B	C	D
Best filter	31.1	23.4	16.9	266	88
λ_{cutoff}	[7.4]	[7.4]	[6.1]	[7.2]	[6.7]
A_b	25.6	19.8	13.9	223	69
A_o	27.5	19.0	15.2	227	83
A_p	29.9	21.8	16.6	255	87
B_b	17.1	11.5	7.2	125	34
B_o	22.3	13.9	9.0	151	42
B_p	21.1	14.2	8.9	153	42

Table 2: Values of f for various filter pairs.

Filters		f for Model			
		A	B	C	D
Baseline filters					
L	B_b	7.1	3.4	63	8.5
M	B_b	6.0	2.9	58	6.4
A_b	B_b	5.2	1.7	43	4.5
Optimum filters					
L	B_o	8.4	4.0	73	10.0
M	B_o	7.0	3.4	67	7.3
A_o	B_o	6.2	2.9	65	7.1
Preferred filters					
L	B_p	8.1	4.0	72	9.9
M	B_p	6.8	3.3	65	7.2
A_p	B_p	5.8	2.6	60	6.4
A_o	B_p	6.0	2.9	64	7.0

Fig. 1

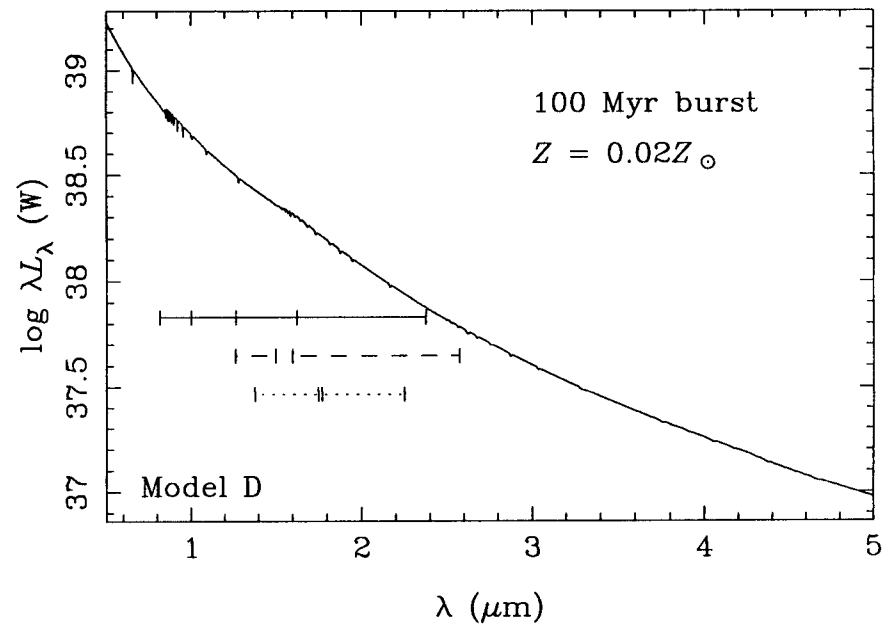
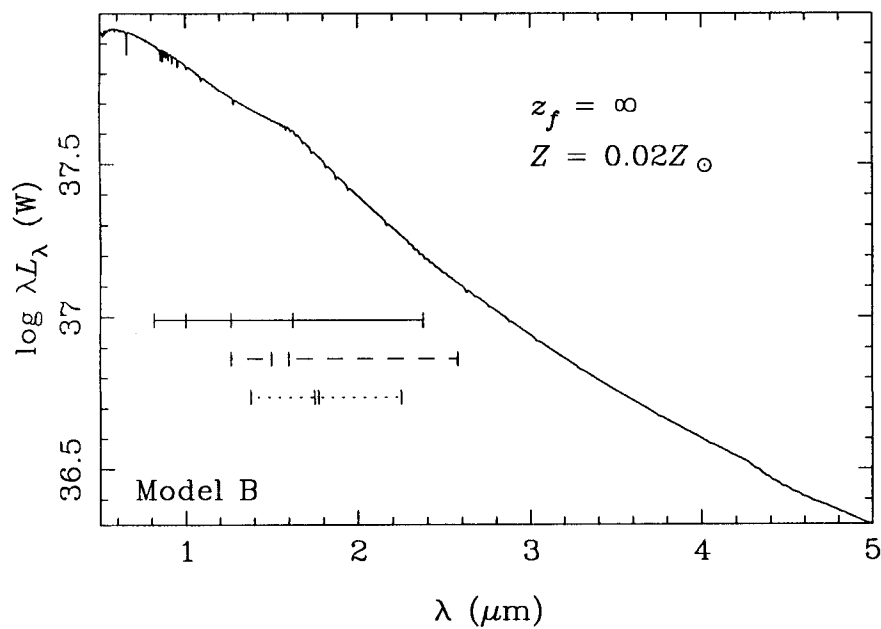
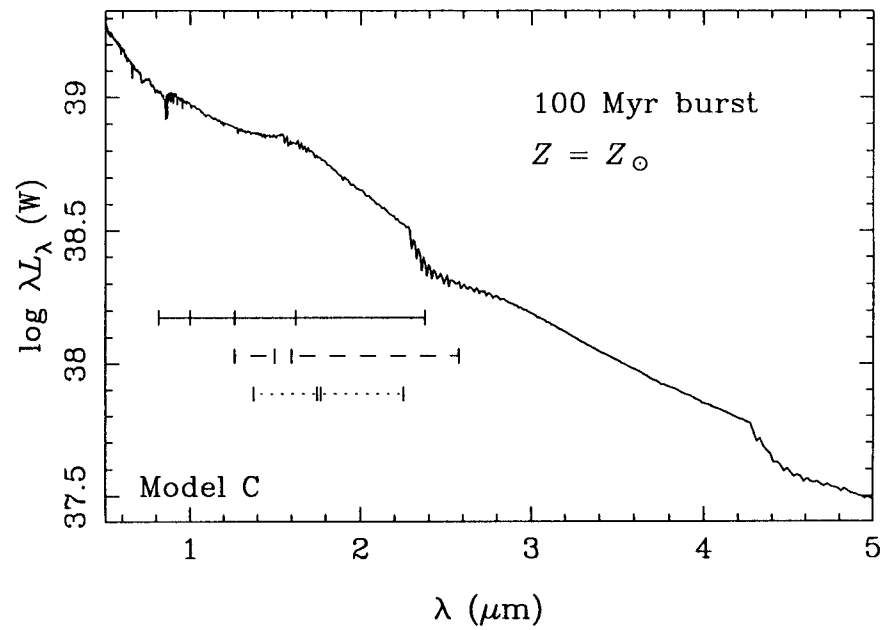
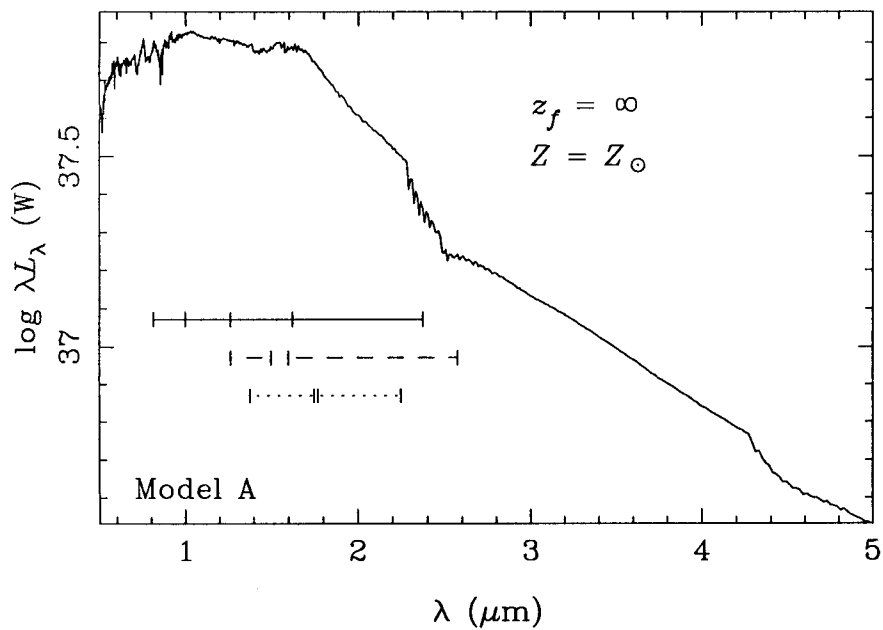


Fig. 2

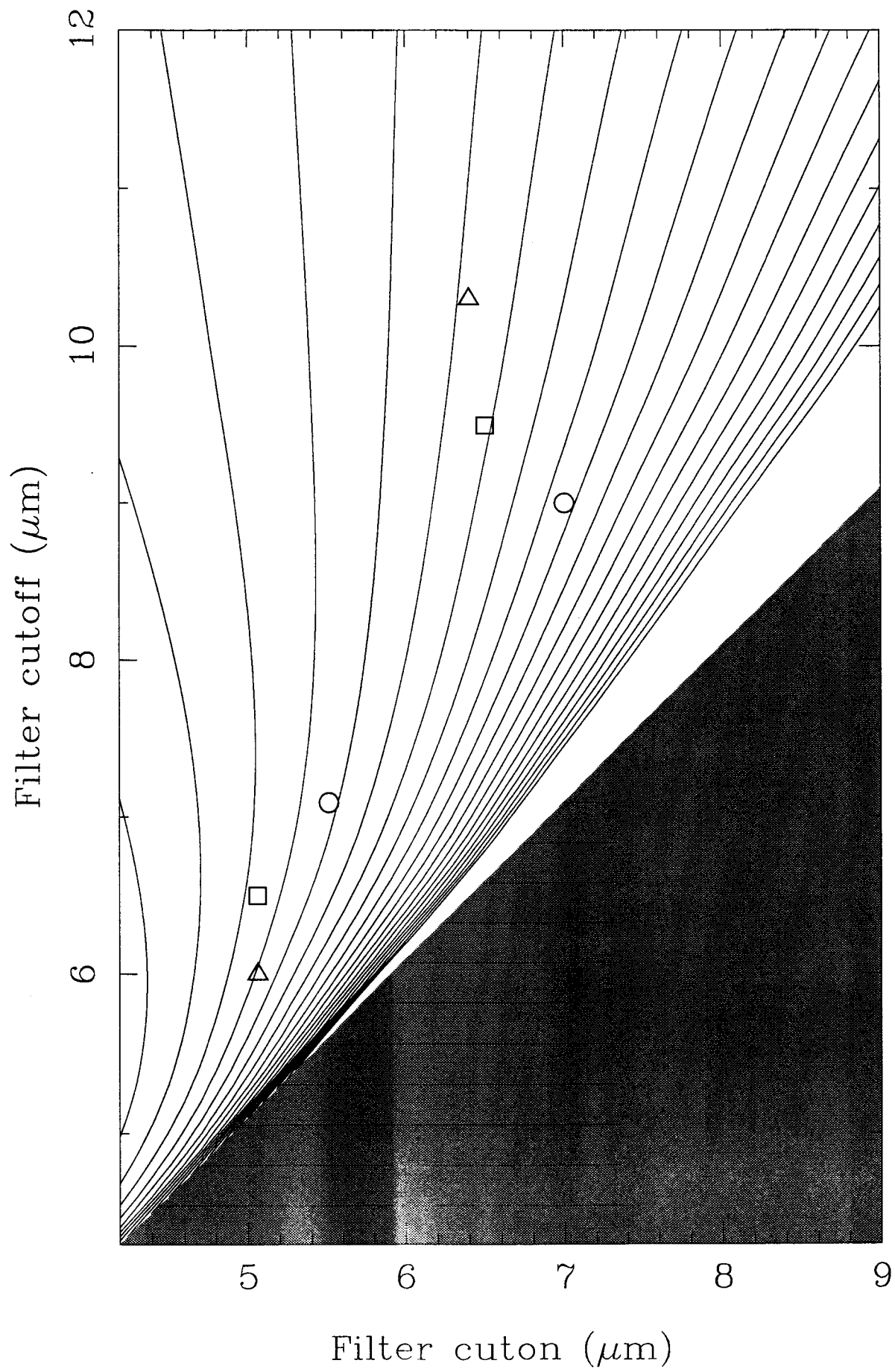


Fig. 3 (left)

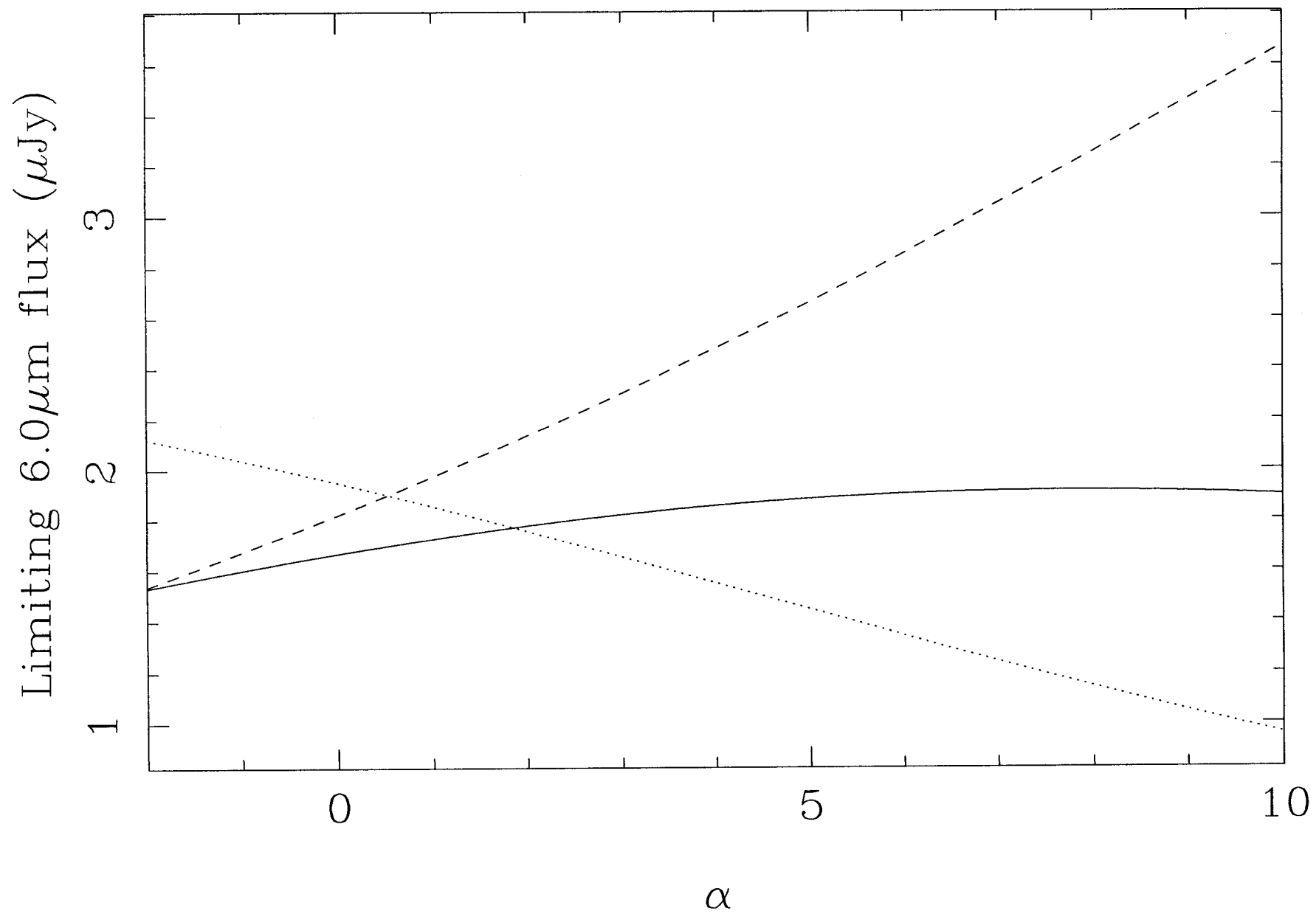
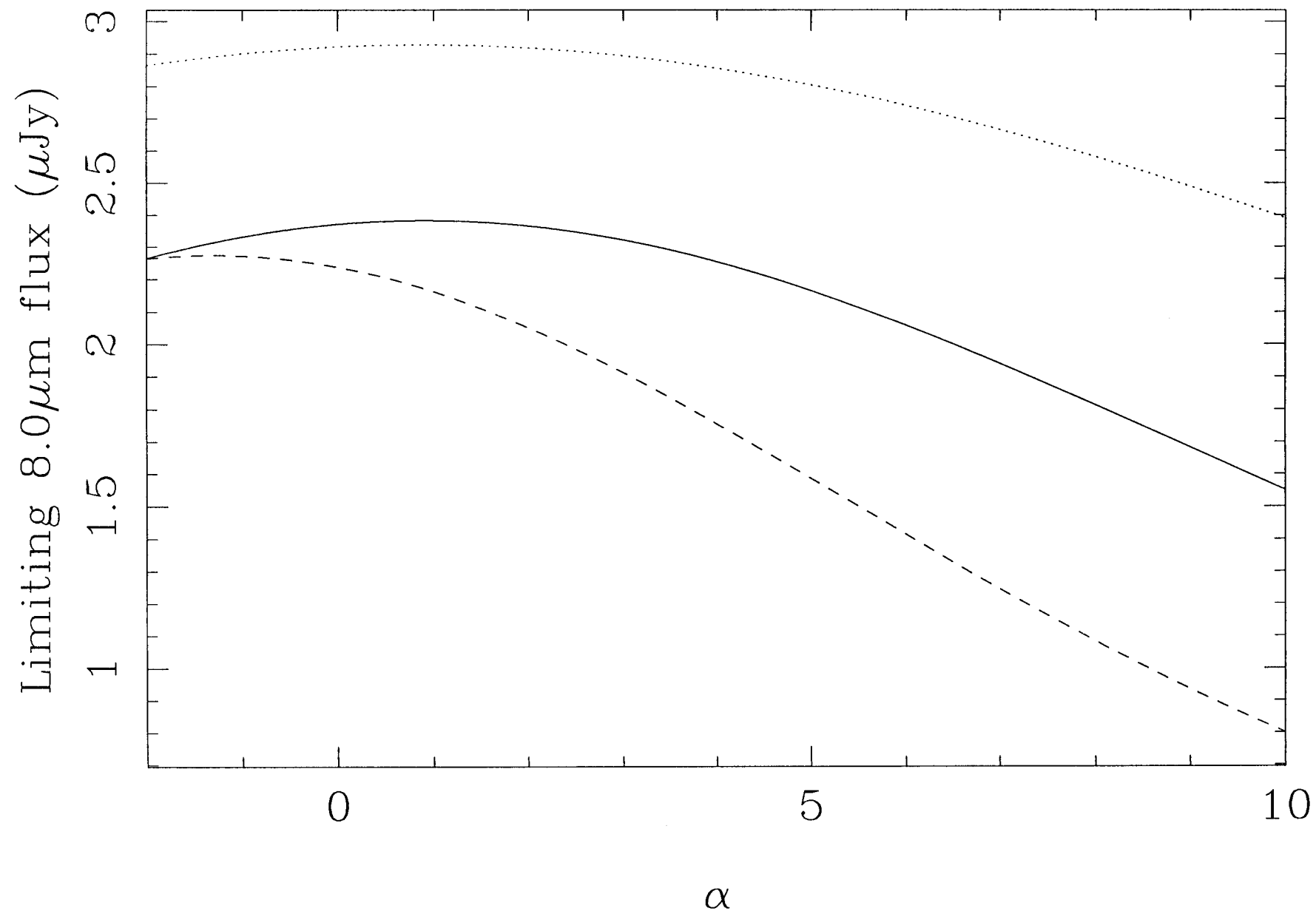


Fig. 3 (right)



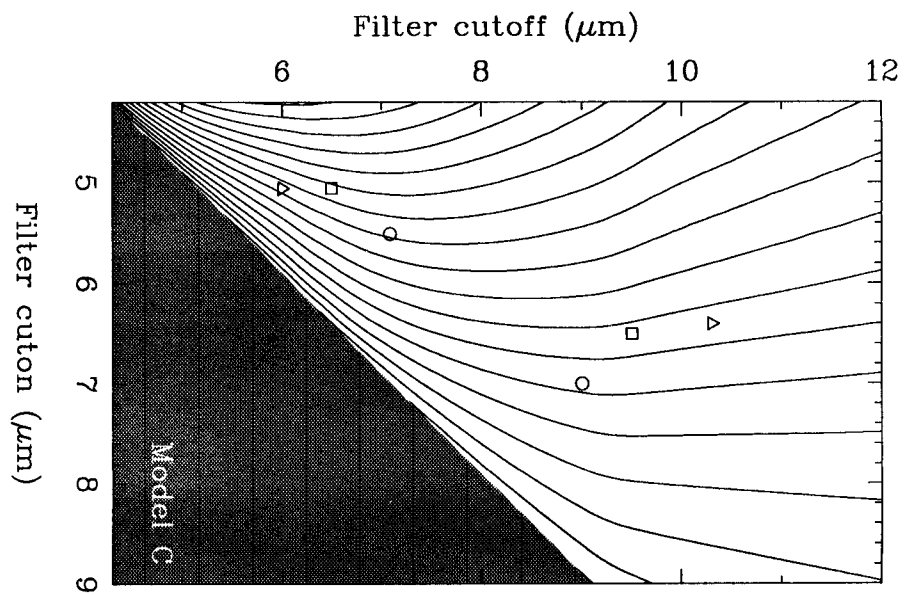
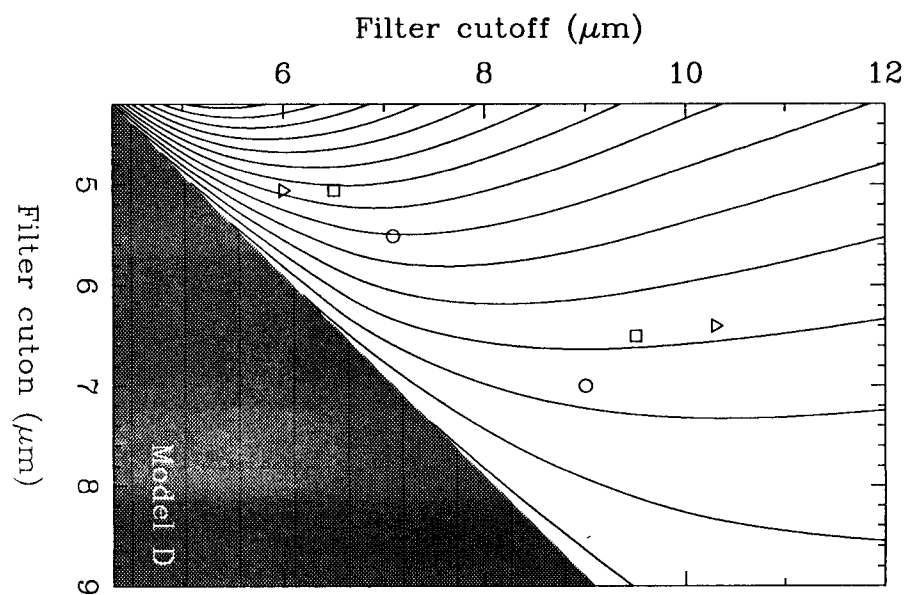
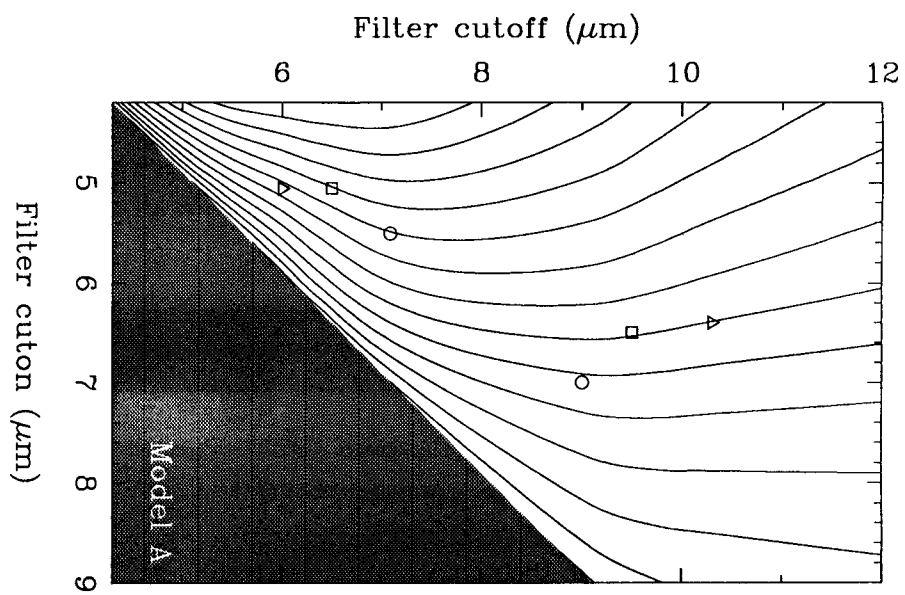
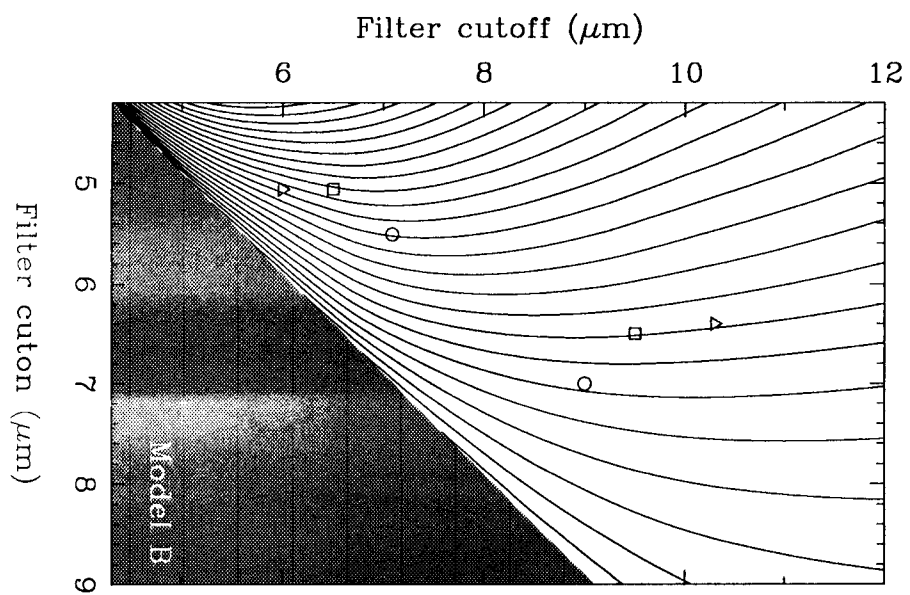


Fig. 4

Fig. 5

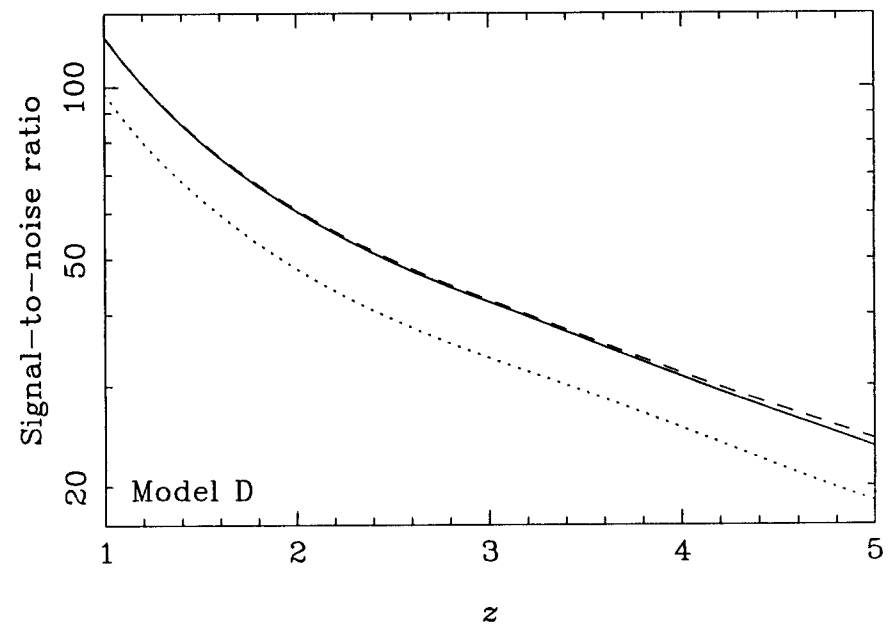
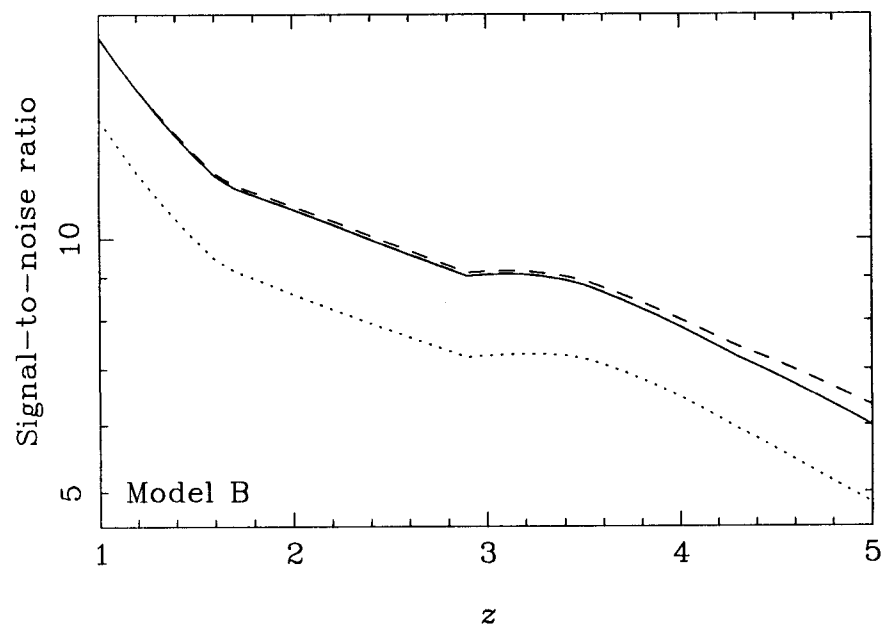
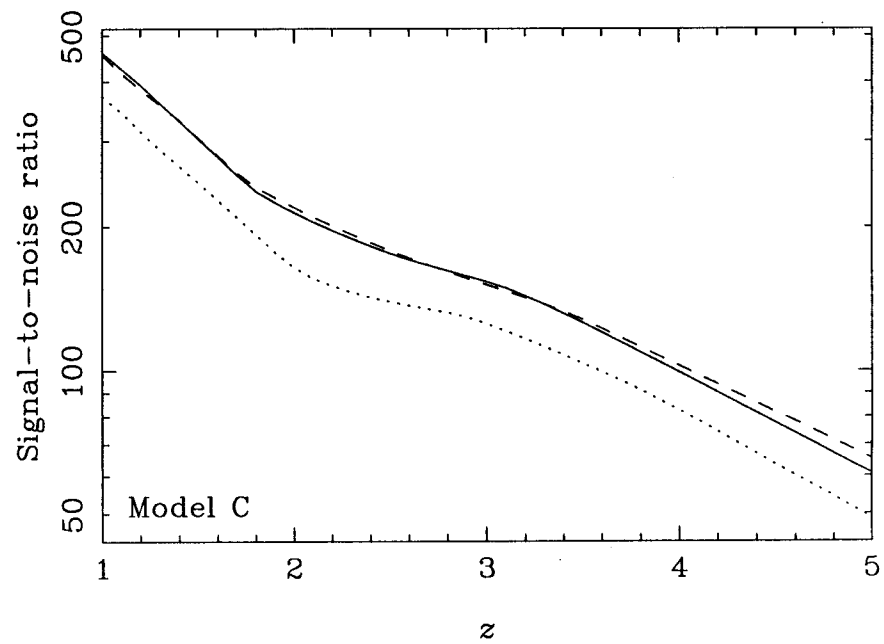
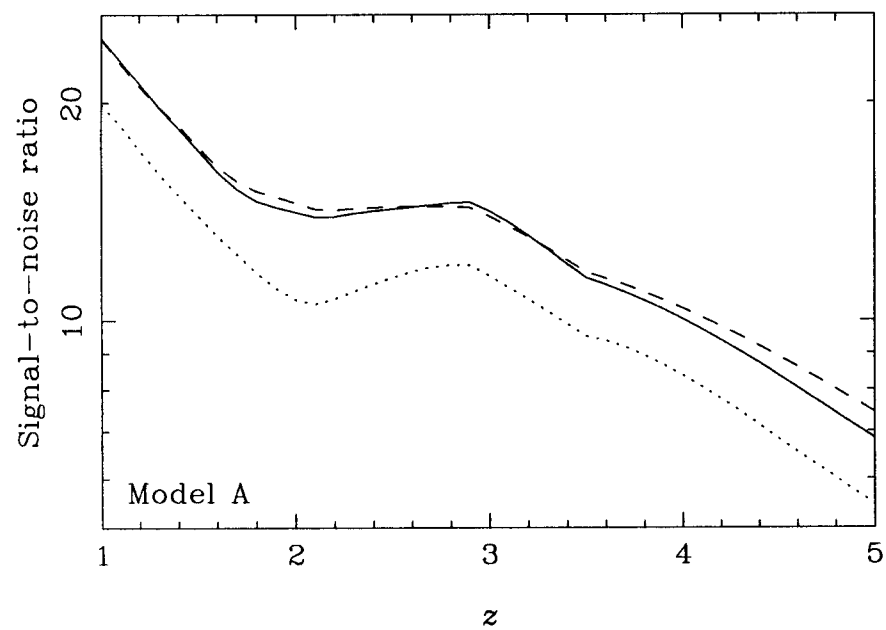


Fig. 6

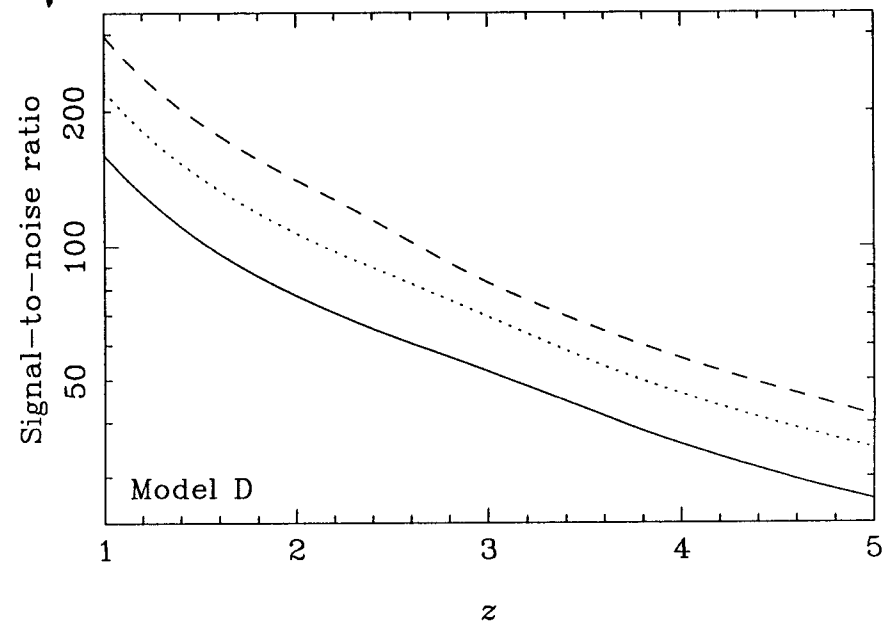
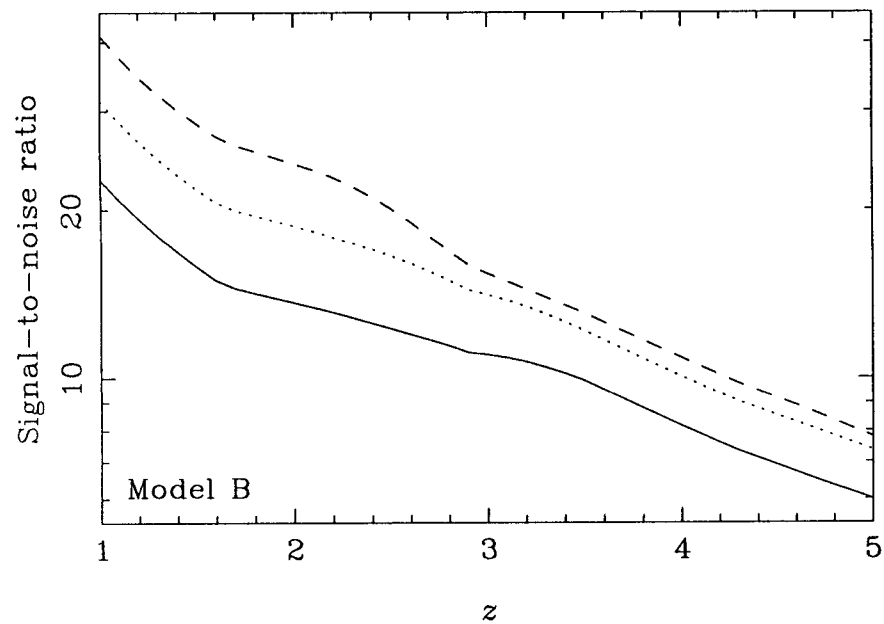
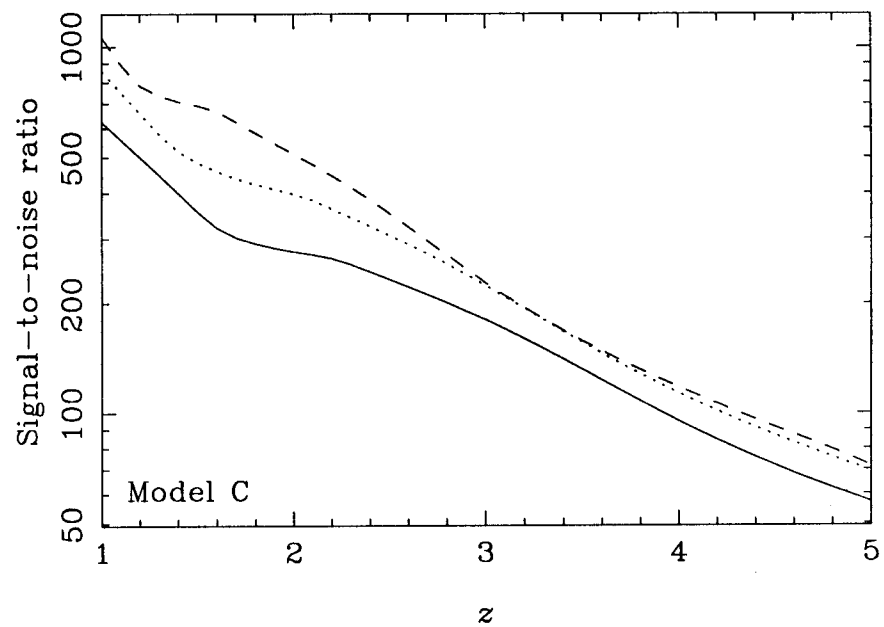
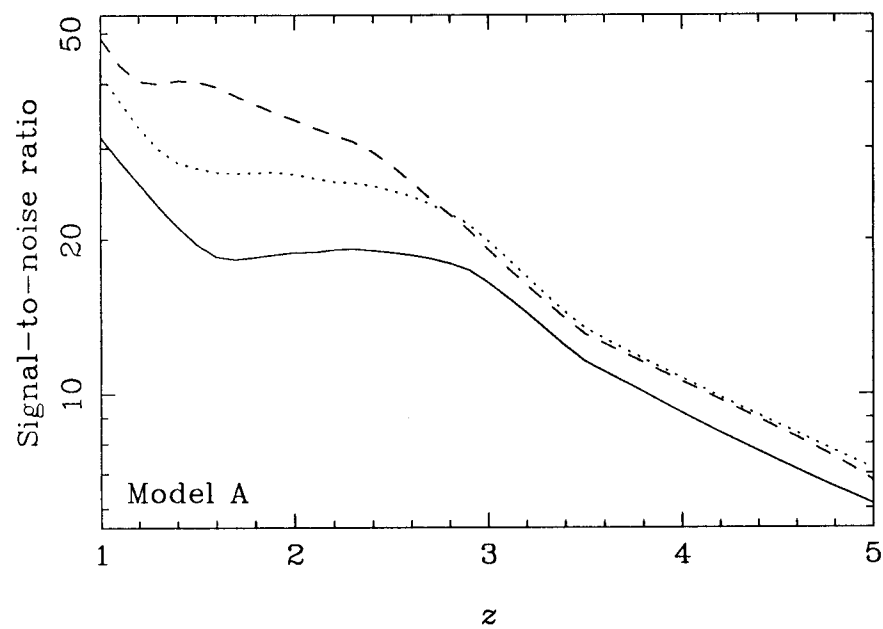


Fig. 7

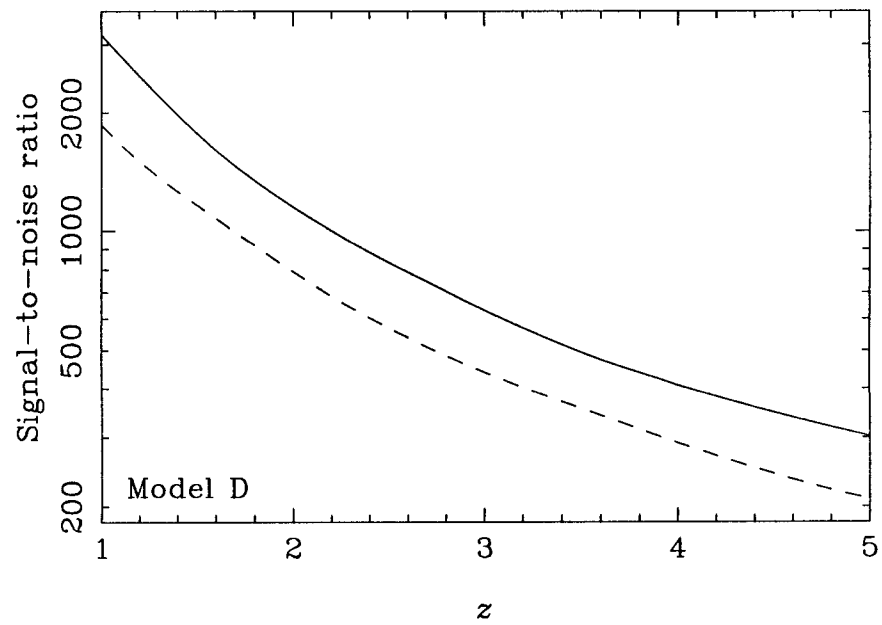
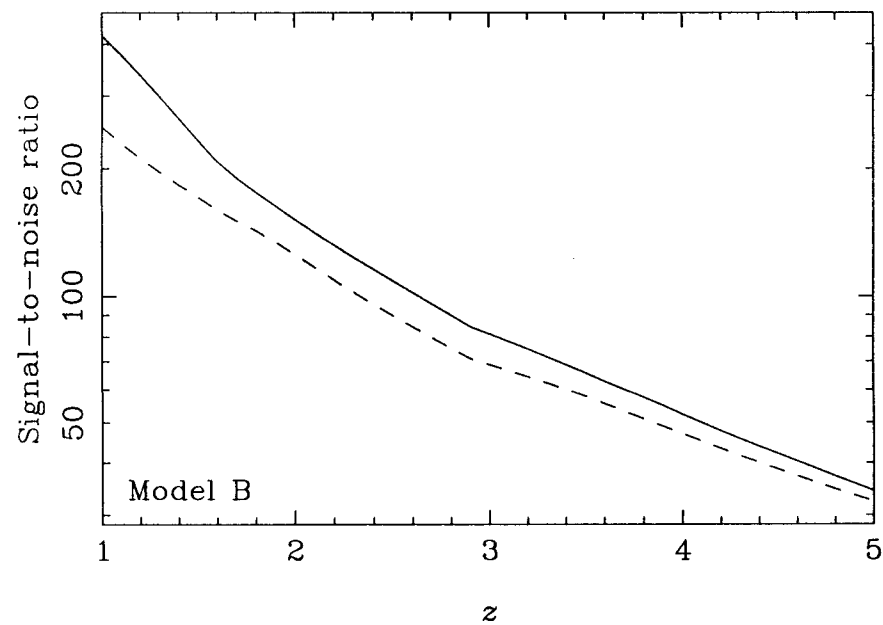
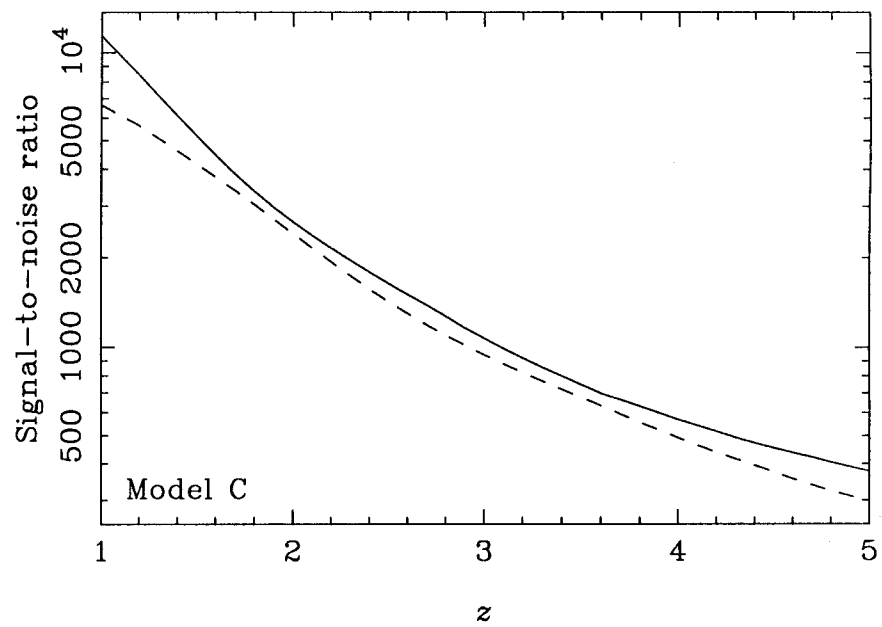
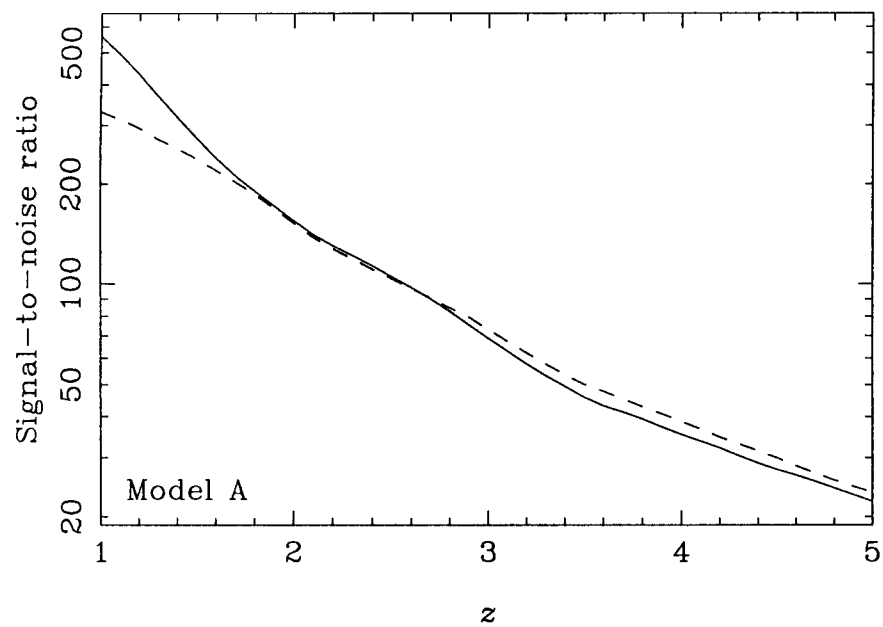


Fig. 8

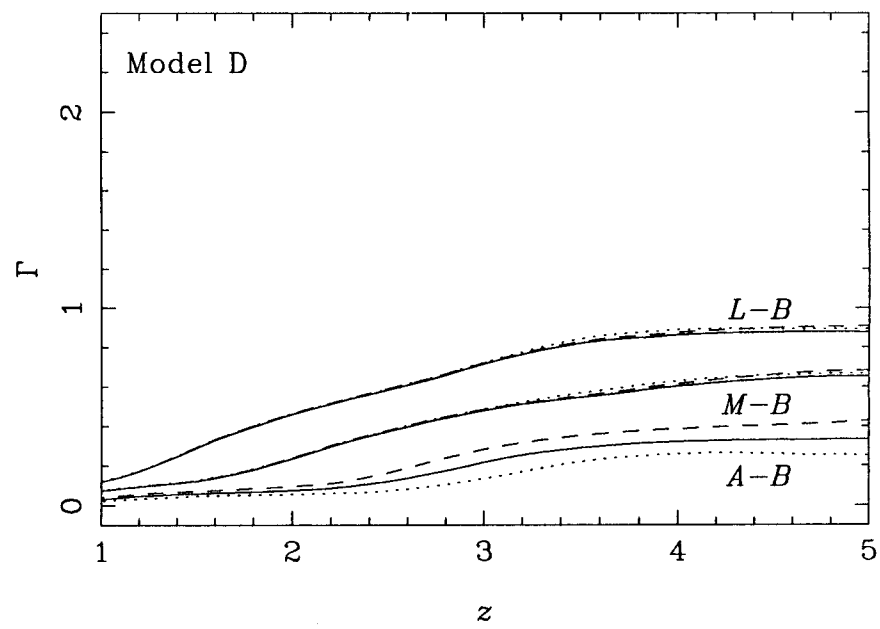
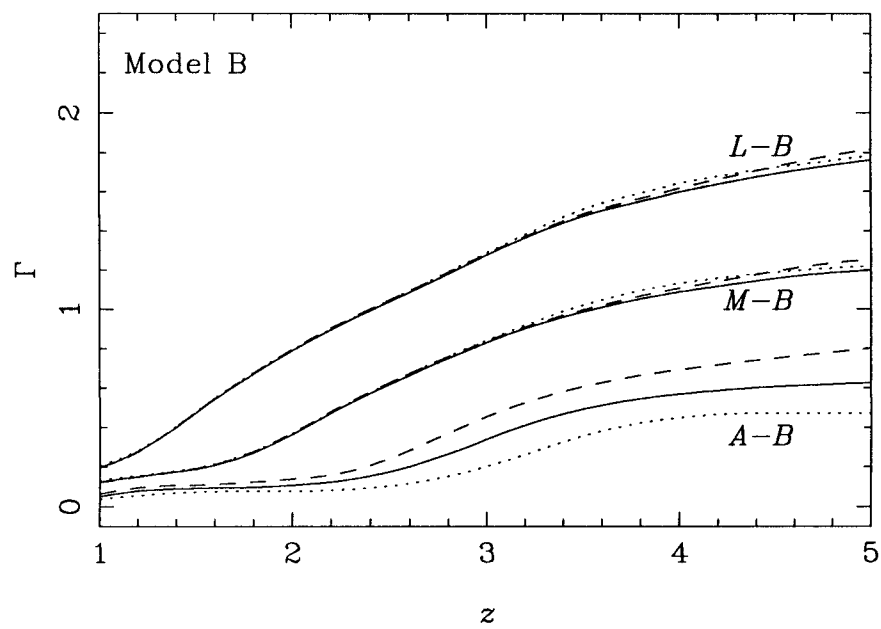
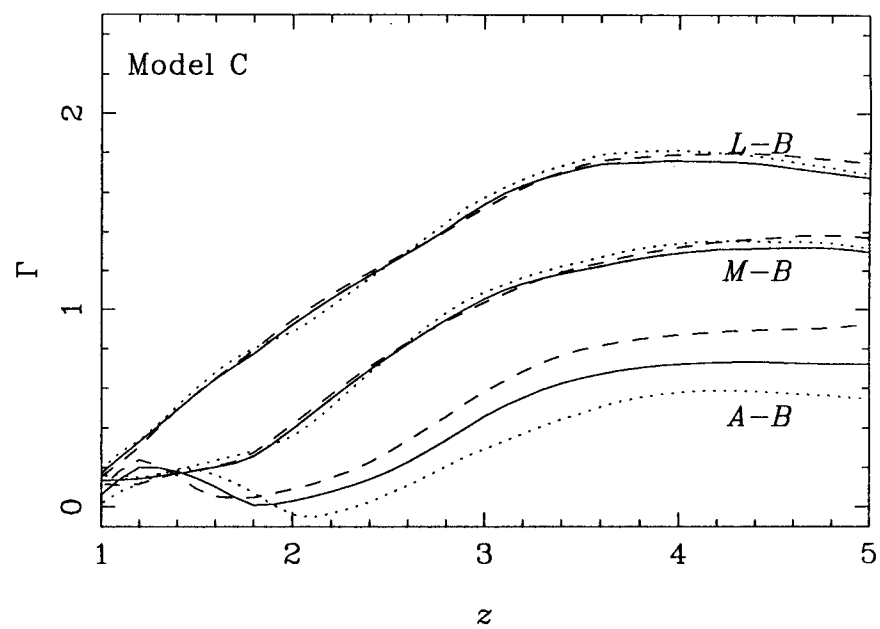
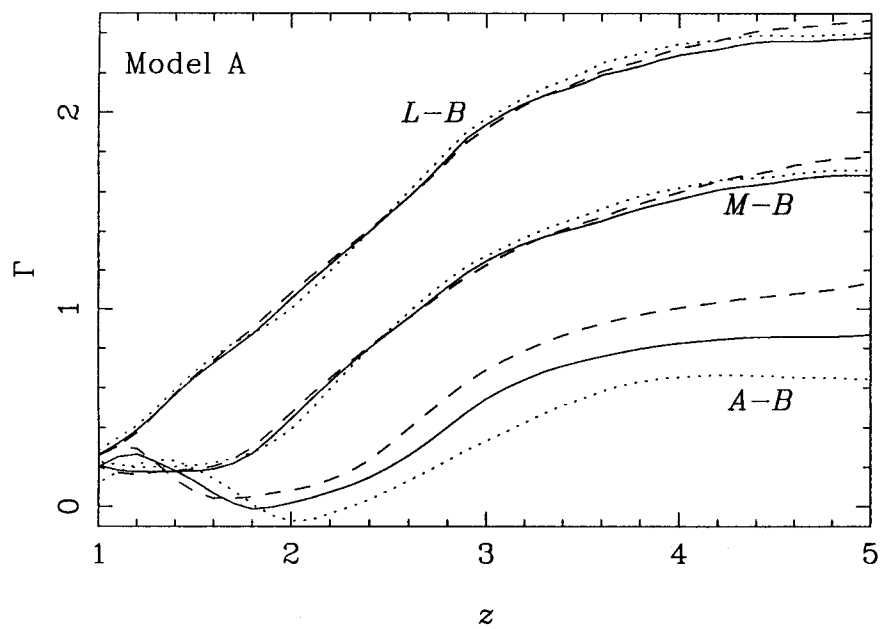


Fig. 9

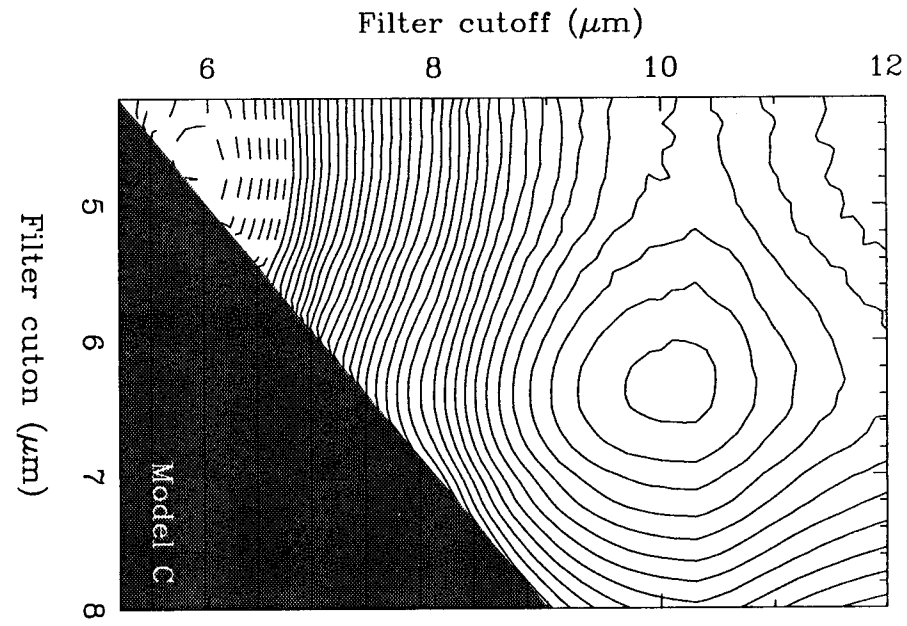
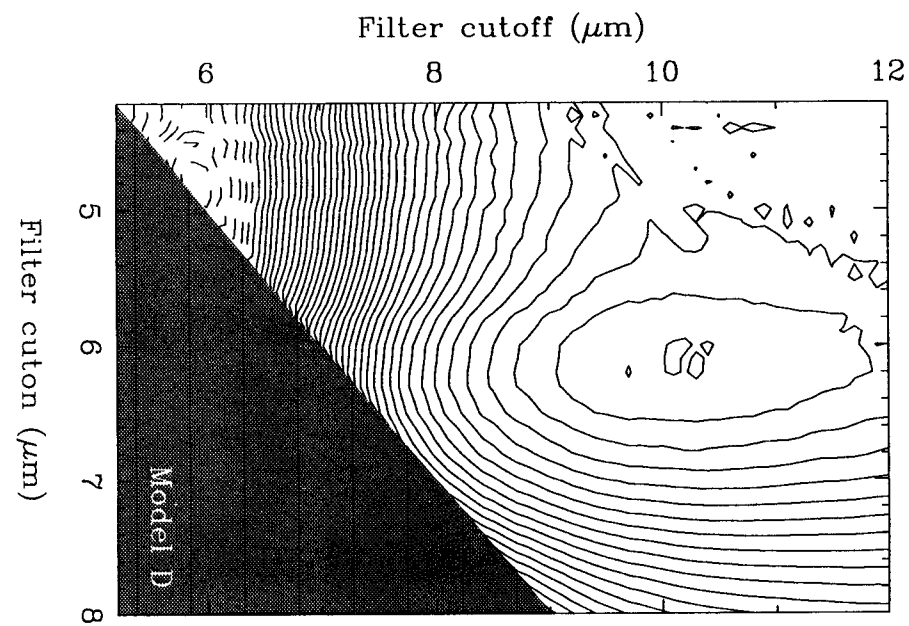
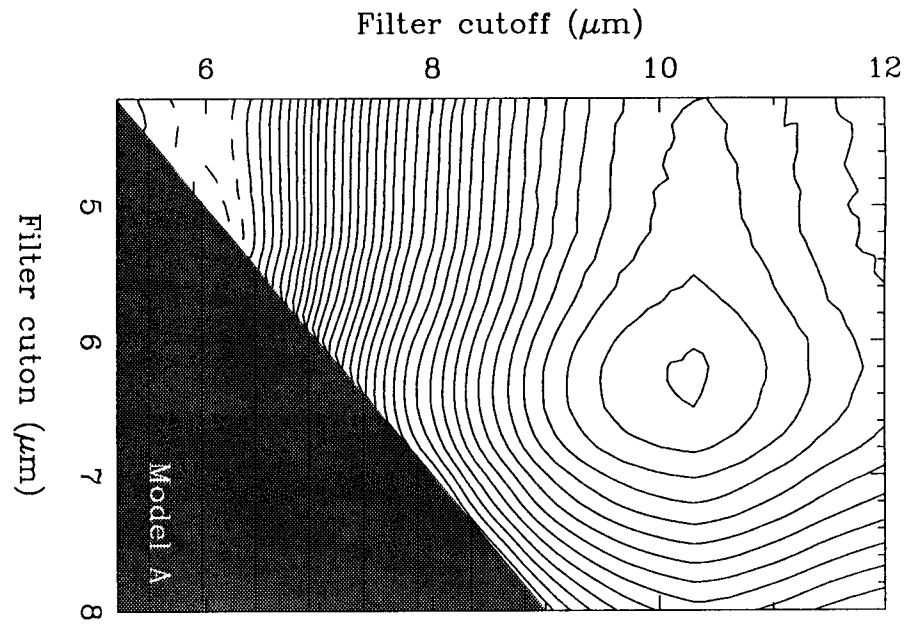
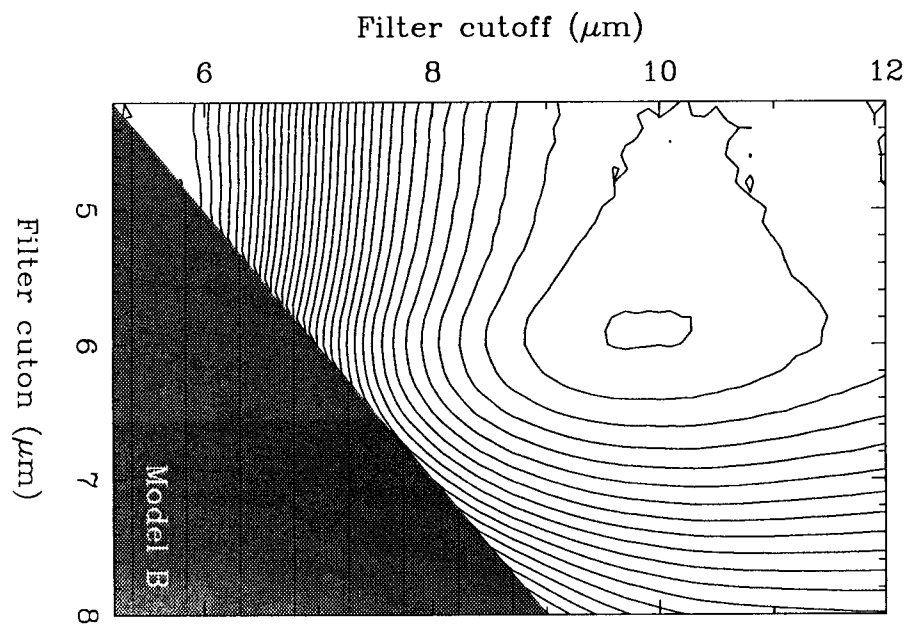


Fig. 10

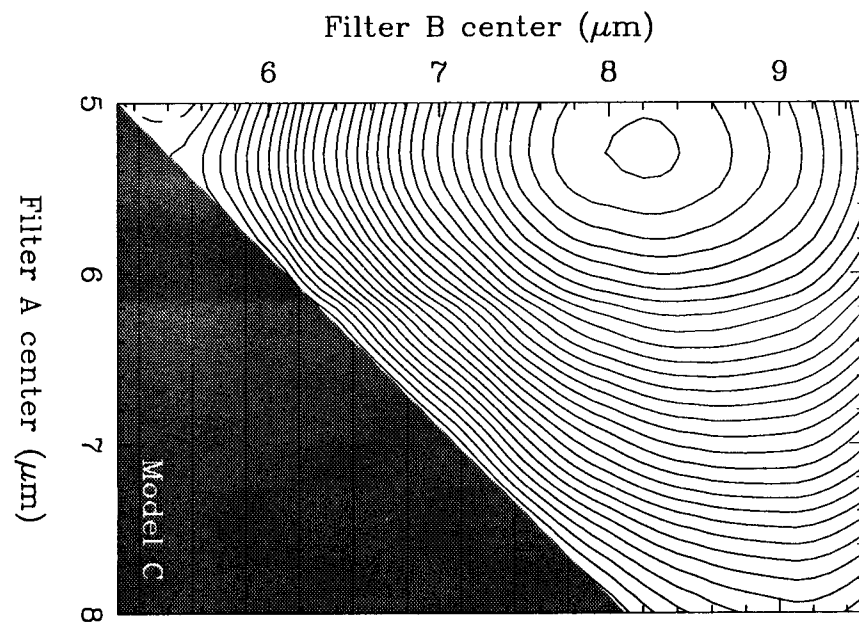
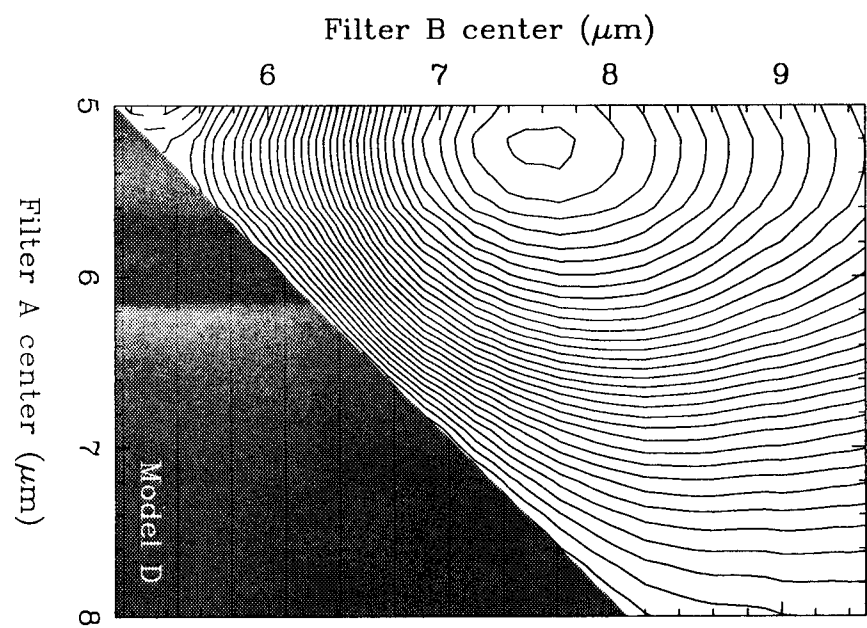
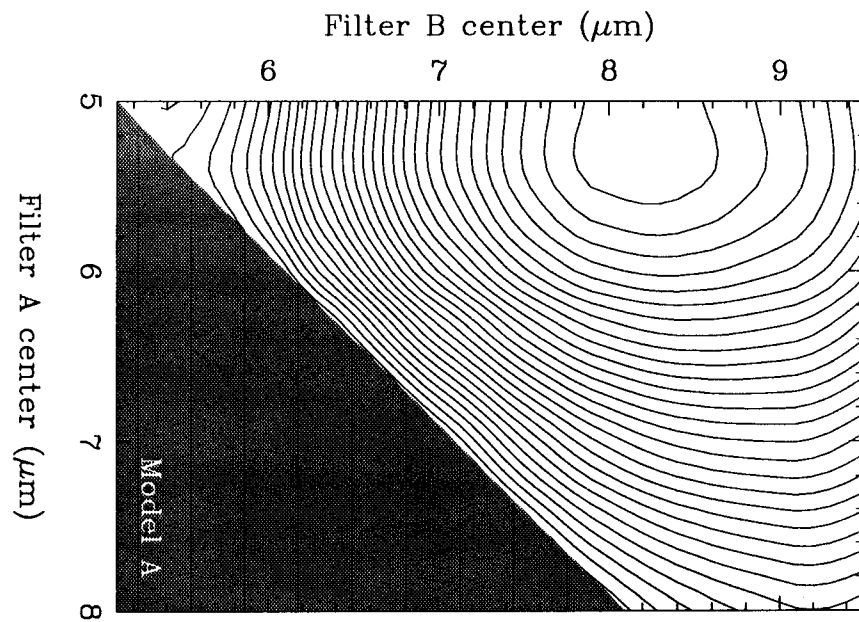
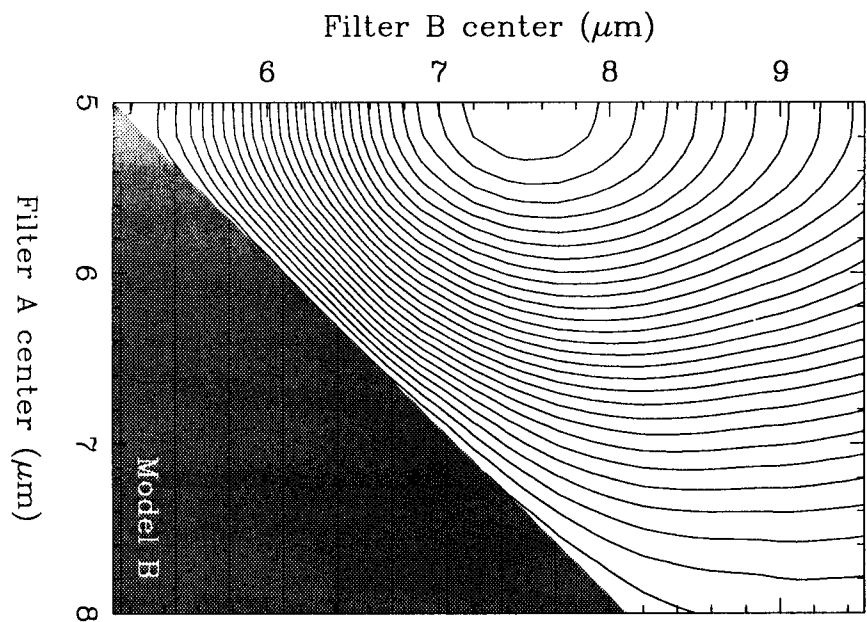


Fig. 11

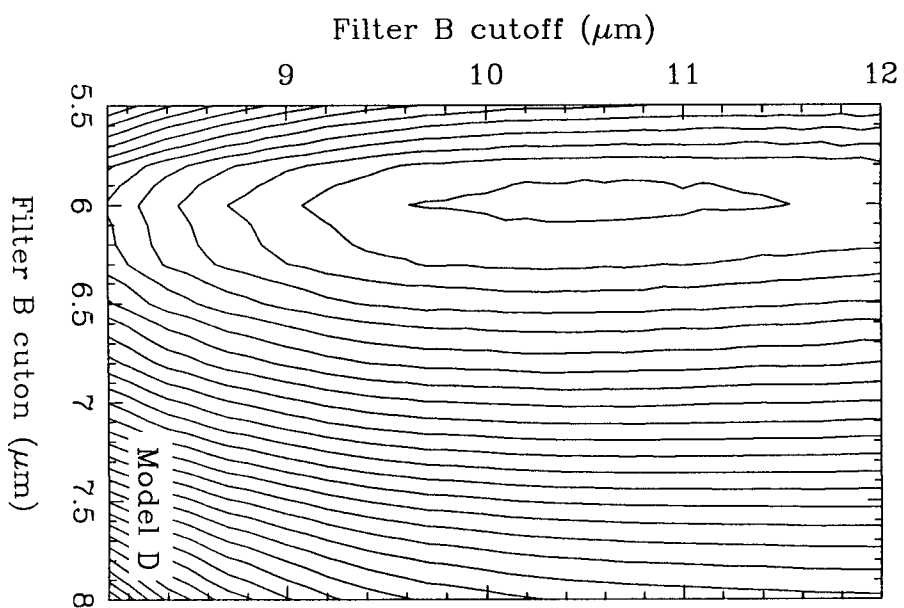
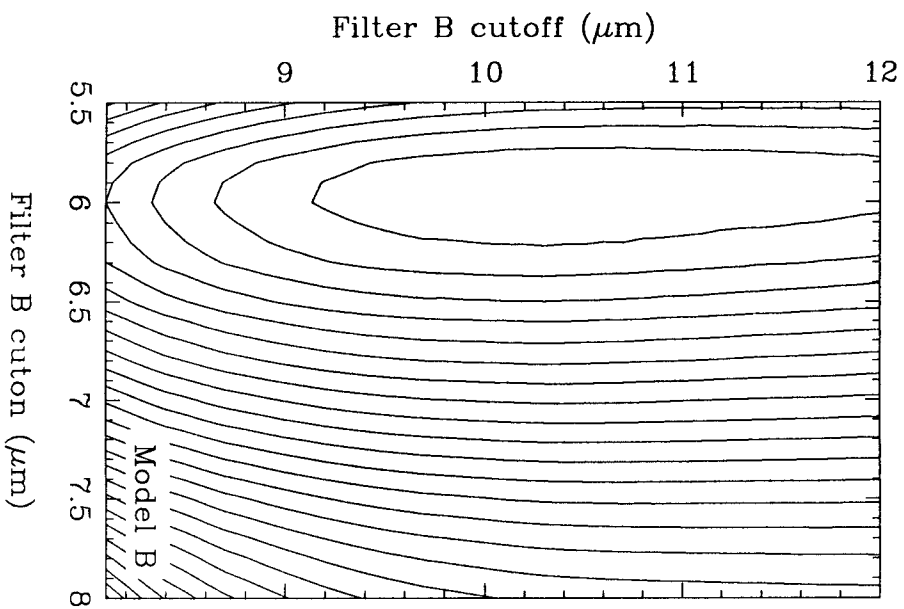
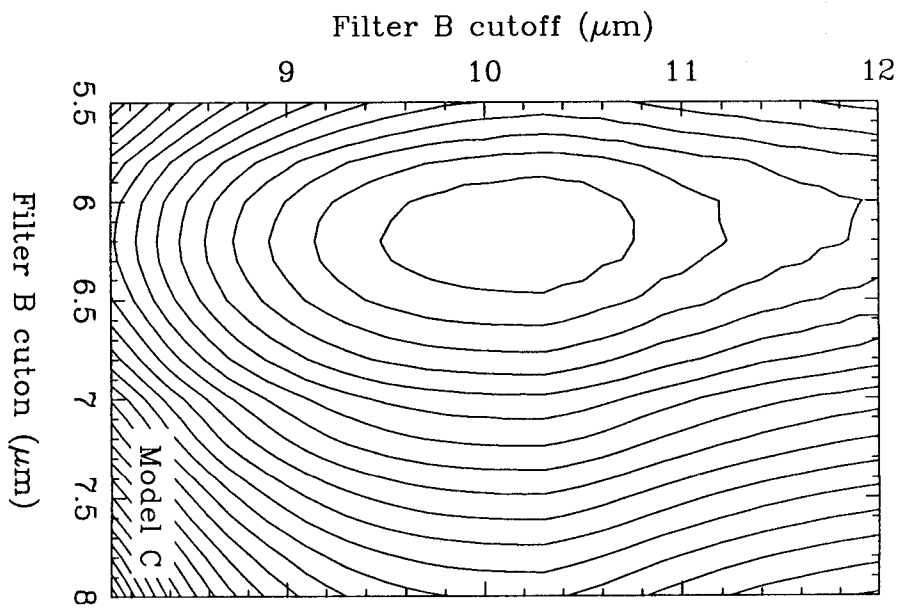
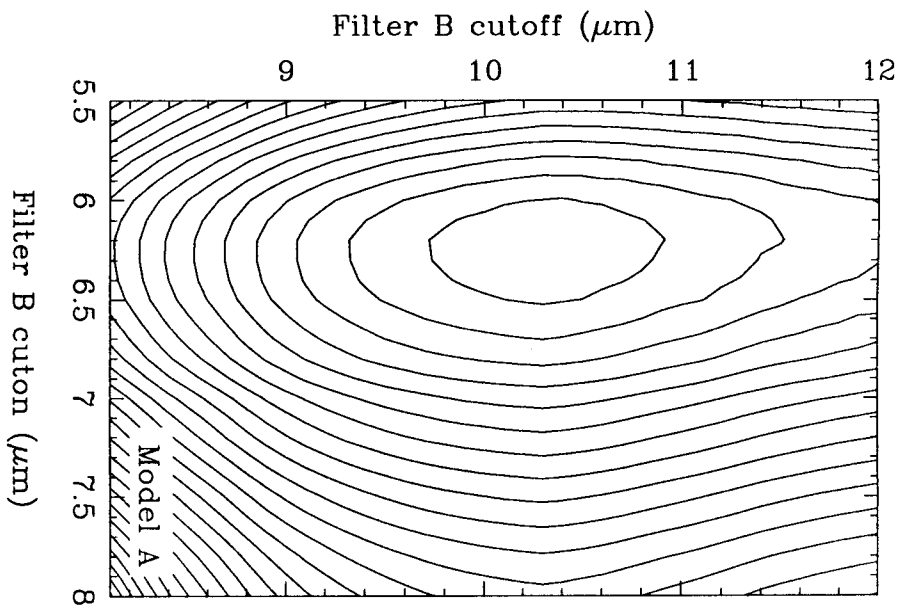


Fig. 12

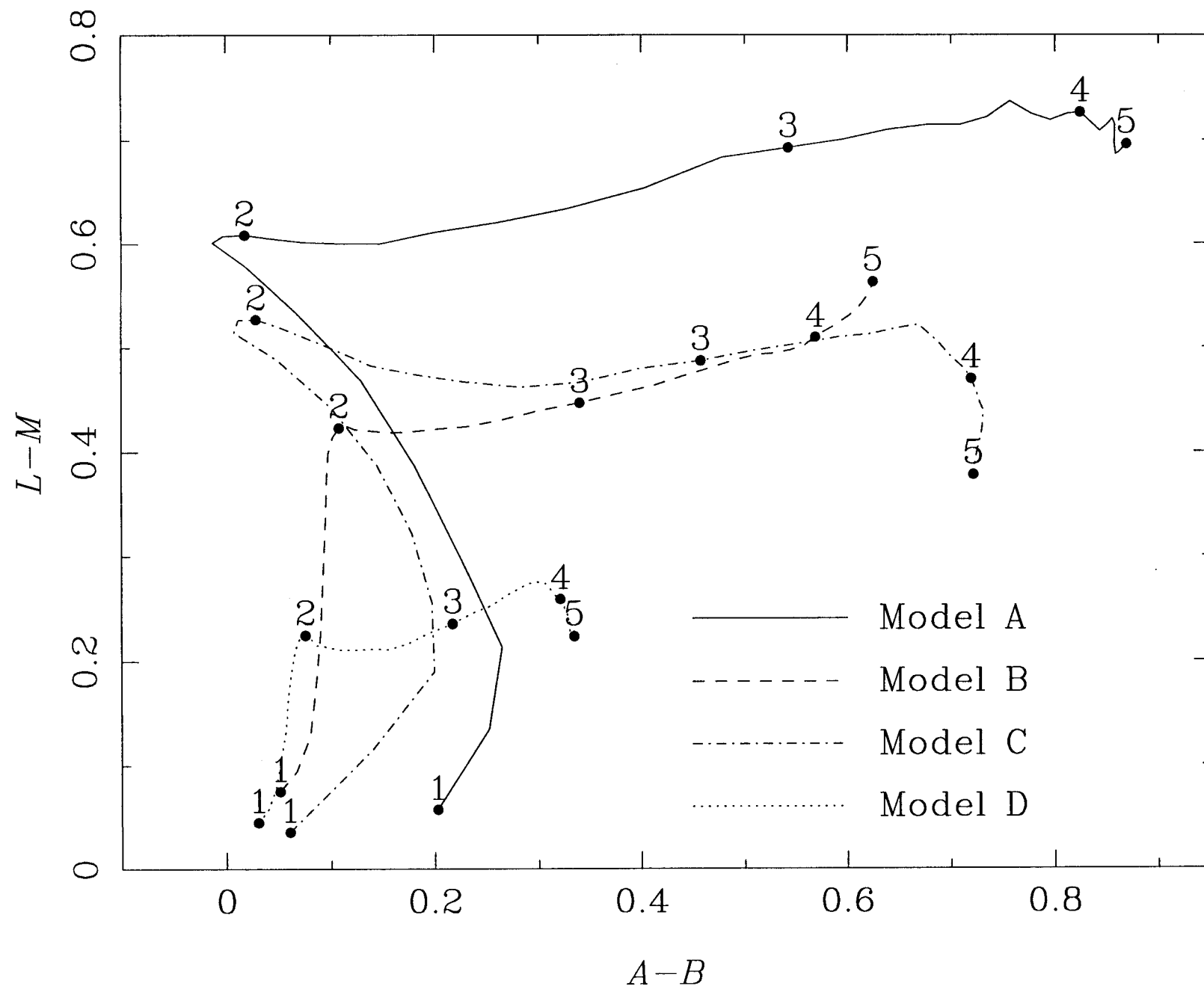


Fig. 13

